Enhanced antiferromagnetic resonance linewidth in NiO/Pt and NiO/Pd

Takahiro Moriyama[1,*] Kensuke Hayashi,[2] Keisuke Yamada[2] Mutsuhiro Shima,[2]
Yutaka Ohya,[2] Yaroslav Tserkovnyak,[3] and Teruo Ono[1]

[1]*Institute for Chemical Research, Kyoto University, Gokasho, Uji, Kyoto 611-0011, Japan*
[2]*Department of Materials Science and Processing, Graduate School of Natural Science and Technology,
Gifu University, Yanagido, Gifu City, Gifu 501-1193, Japan*
[3]*Department of Physics and Astronomy, University of California, Los Angeles, California 90095, USA*

In this paper, we investigate the enhancement of the antiferromagnetic damping in the sintered NiO-HM (where HM is heavy metal) granular systems having NiO/HM interfaces, where HM = Pt or Pd. Under the assumption of the spin pumping model, we derive the effective interfacial damping conductance g_{eff}, the parameter which characterizes the upper-bound estimate of the spin pumping effect, to be $12 \pm 1 \, nm^{-2}$ and $5 \pm 1 \, nm^{-2}$ for the NiO/Pt and the NiO/Pd interfaces, respectively, at room temperature. g_{eff} experimentally derived in this study are an important milestone in antiferromagnetic spintronics, giving a guideline for various spin current transfer and spin interaction phenomena with antiferromagnets where the spin mixing conductance is involved.

A flow of electron spins, or spin current, exerts a torque on the local magnetization as an important consequence of the interplay between the local magnetizations and the itinerant electron spins [1]. By this so-called spin torque effect, one can manipulate the magnetization directions [2] and even excite a persistent magnetization dynamics [3]. Most recently, it has been demonstrated that the same operation principle can be applied to antiferromagnets which have no net magnetization but rather staggered microscopic spins [4–7]. The spin torque effect is much appreciated in modern spintronic applications [8], such as memory, logic, and high-frequency devices, as it requires much less energy to control the magnetization when comparing to the traditional Ampère field.

On the other hand, the magnetization dynamics can create a flow of spin current as a reciprocal process of the spin torque effect [9]. This so-called spin pumping effect ejects the spin current (without any net charge current) into an adjacent material in contact with the magnetic material under the magnetization dynamics. A consequence of the spin pumping effect becomes noticeable when a nonmagnetic heavy metal (HM) with strong spin-orbit interaction is in contact, such as Pt or Pd. One of the significant consequences is a broadening of the magnetic resonant linewidth [10]. When the pumped spin current is dissipated by the adjacent material, the loss of the spin current, or the loss of the spin angular momentum, results in an enhancement of damping of the magnetic system and therefore the increase of the resonant linewidth. Alternatively, the pumped spin current can be electrically detected via the inverse spin Hall effect (ISHE) [11], which adds a great potential to the spin pumping effect not only toward application [12] but also for a sensitive probe of various spin-orbit related phenomena [13,14].

Since it is generally convenient to excite steady magnetization dynamics in order to observe the spin pumping effect, almost all the spin pumping experiments have so far been investigated with ferromagnetic materials at the ferromagnetic resonant frequency in a gigahertz range by using well-established microwave electronics. However, in conjunction with the recently emerging antiferromagnetic spintronics [15,16], there is a growing interest in the spin pumping effect in antiferromagnetic materials with the Néel order dynamics in a terahertz (THz) frequency range [17–20], which can open up a new realm of *THz* spintronics leading to novel THz spin devices [21,22] and leading to an improved understanding of the ultrahigh-speed spin phenomena in magnetism. While the spin pumping effect in ferromagnets is well understood from both experimental and theoretical points of view, the lack of experimental demonstrations of the antiferromagnetic spin pumping effect, in spite of recent intensive theoretical efforts [17–20], impedes further advancement of antiferromagnetic spintronics toward THz spintronics.

In this Rapid Communication, we investigate the enhanced damping in antiferromagnets at the THz resonant frequency. The cw-THz spectroscopy revealed that the magnetic damping of the sintered NiO-HM granular systems, where HM = Pt or Pd, is enhanced due to the NiO/HM interface, which suggests the spin pumping effect. The effective interfacial damping conductance g_{eff}, derived under assumption that the whole damping enhancement would be due to the spin pumping effect, is found to be $g_{eff} = 12 \pm 1 \, nm^{-2}$ and $5 \pm 1 \, nm^{-2}$ for the NiO/Pt and the NiO/Pd interfaces, respectively, at room temperature. The trend of g_{eff} is consistent with the ferromagnetic/HM case where the Pd interface generally exhibits smaller g_{eff} than the Pt interface [9,23,24].

First, we try to formulate the damping variation, under the assumption of the spin pumping model, with antiferromagnetic NiO and the HM as depicted in Fig. 1(a). NiO is antiferromagnetic below the Néel temperature $T_N = 523$ K and is a rocksalt structure with a slight rhombohedral distortion [25]. In the ground state, the Ni^{2+} spins align ferromagnetically in a {111} plane and are antiferromagnetically coupled
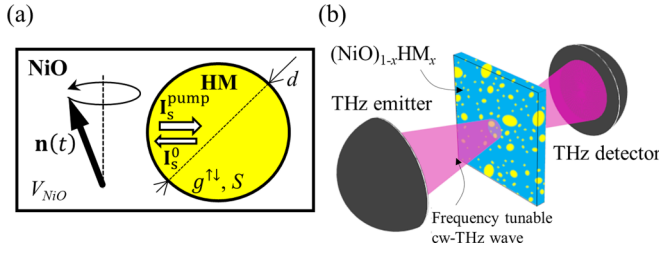
FIG. 1. THz spectroscopy measurements and spin pumping in the NiO/HM system. (a) The precessing Néel order $\mathbf{n}(t)$ in the NiO with the volume V_{NiO} pumps the spin current $\mathbf{I}_s^{pump}$ into the HM with the contact area S and the effective spin mixing conductance $g_s^{\uparrow\downarrow}$. The resulting backflow spin current $\mathbf{I}_s^0$ in turn flows back into the NiO. (b) Schematic illustration of the cw-THz spectroscopy setup measuring the THz wave transmission through the $(NiO)_{1-x}HM_x$ samples.

between adjacent {111} planes, resulting in a strong *easy-plane* anisotropy in a {111} plane and a weak threefold *in-plane* anisotropy in the $\langle 11\bar{2} \rangle$ directions in the {111} plane.

Magnetization dynamics of the antiferromagnetic NiO can be described by the following Lagrangian density based on the conventional sigma model [26,27],

$$\mathcal{L}[\mathbf{n}] = \frac{\chi_\perp}{2}(\partial_t\mathbf{n} + \mathbf{n} \times \gamma\mathbf{B})^2 - \frac{A}{2}(\partial_t\mathbf{n})^2 - \frac{K_1 n_x^2 + K_2 n_y^2}{2}, \quad (1)$$

where $|\mathbf{n}| \equiv 1$ is the directional Néel order and K_1 and K_2 are the out-of-easy-plane and in-plane anisotropy energies, respectively, with $K_1 \gg K_2$. Note that in the Cartesian coordinate we set the y-z plane as the easy plane within which the Néel order prefers to orient along the z axis. $\gamma = 1.76 \times 10^{11}$ T^{-1} s^{-1} is the gyromagnetic ratio and $\chi_\perp$ is the perpendicular spin susceptibility. $\mathbf{B}$ is the applied magnetic field. The Lagrangian leads to two linearly polarized modes governed by K_1 and K_2. Below, we focus on the higher-frequency mode due to K_1 and discuss the magnetic dynamics in the absence of a static magnetic field, in line with our experimental results. Our linewidth analysis, however, is independent of the anisotropy and thus insensitive to the precise mode identification. The dissipation is described by the following Rayleigh function [28],

$$\mathcal{R}[\partial_t\mathbf{n}] = \frac{\alpha s}{2}(\partial_t\mathbf{n})^2, \quad (2)$$

where

$$\alpha = \alpha_0 + \frac{\hbar g_{eff}^{\uparrow\downarrow}}{4\pi s}\frac{S}{V_{NiO}}. \quad (3)$$

α_0 is the intrinsic damping. The second term representing the spin pumping enhanced damping is derived from the total spin current dissipation $\mathbf{I}_s$, which is the sum of the pumped spin current $\mathbf{I}_s^{pump}$ and the backflow spin current $\mathbf{I}_s^0$ as $\mathbf{I}_s = \mathbf{I}_s^{pump} + \mathbf{I}_s^0$ [see Fig. 1(a)]. $g_{eff}^{\uparrow\downarrow}$ is the effective spin mixing conductance at the NiO/HM interface solely characterizing the spin pumping effect, s is the full saturated spin density of magnetic sublattices, S is the interface area, and V_{NiO} is the volume of the NiO. By solving the Euler-Lagrange equation with the Lagrangian density in Eq. (1) and the dissipation term in Eq. (2), the (linearly polarized) small-angle Néel vector dynamics can eventually be written as the damped oscillator equation as [29]

$$\ddot{n} + \Delta\omega\dot{n} + \omega^2 n = 0, \quad (4)$$

where the resonant frequency ω and the resonant linewidth (full width at half maximum) $\Delta\omega$ are, respectively,

$$\omega = \sqrt{K_1/\chi_\perp} \quad (5)$$

and

$$\Delta\omega = \alpha s/\chi_\perp. \quad (6)$$

With Eqs. (3) and (6), we can therefore characterize the spin pumping effect from the resonant linewidth of the antiferromagnetic resonance.

The samples used in this experiment are sintered pellets of NiO with the inclusion of HM granules, referred to as the NiO-HM granular pellets, synthesized from a mixture of NiO and Pt or Pd powder [see Supplemental Material (SM) for a detailed sample preparation procedure [29]]. We vary the S/V_{NiO} ratio by varying the composition of the pellets to be $(NiO)_{1-x}HM_x$ ($x = 0$, 0.02, 0.05, 0.08, and 0.10). We hereafter refer to Pt and Pd compositions as x_{Pt} and x_{Pd}, respectively. Table I shows the packing ratio for each pellet, which is the ratio of the measured pellet density to the nominal density calculated for the given composition of NiO (6.67 g/cm³), Pt (21.5 g/cm³), and Pd (12.0 g/cm³). The packing ratio less than unity indicates that the pellets contain air pores. We also prepared some control samples, in which the air pore composition x_p of the NiO pellet is deliberately varied [29], in order to elucidate the effect of the HM granules by comparing with the *air granules*, i.e., air pores. THz wave transmission through the granular pellets was measured by using a frequency domain cw-THz spectroscopy system [30,31] capable of scanning up to 2 THz as the schematic illustration shows in Fig. 1(b). The absorption peak due to the antiferromagnetic resonance is expected in the transmission spectra. The temperature of the sample can be controlled

TABLE I. Packing ratio and average dimeter of the Pt and Pd granules for various compositions x_{Pt} and x_{Pd}.

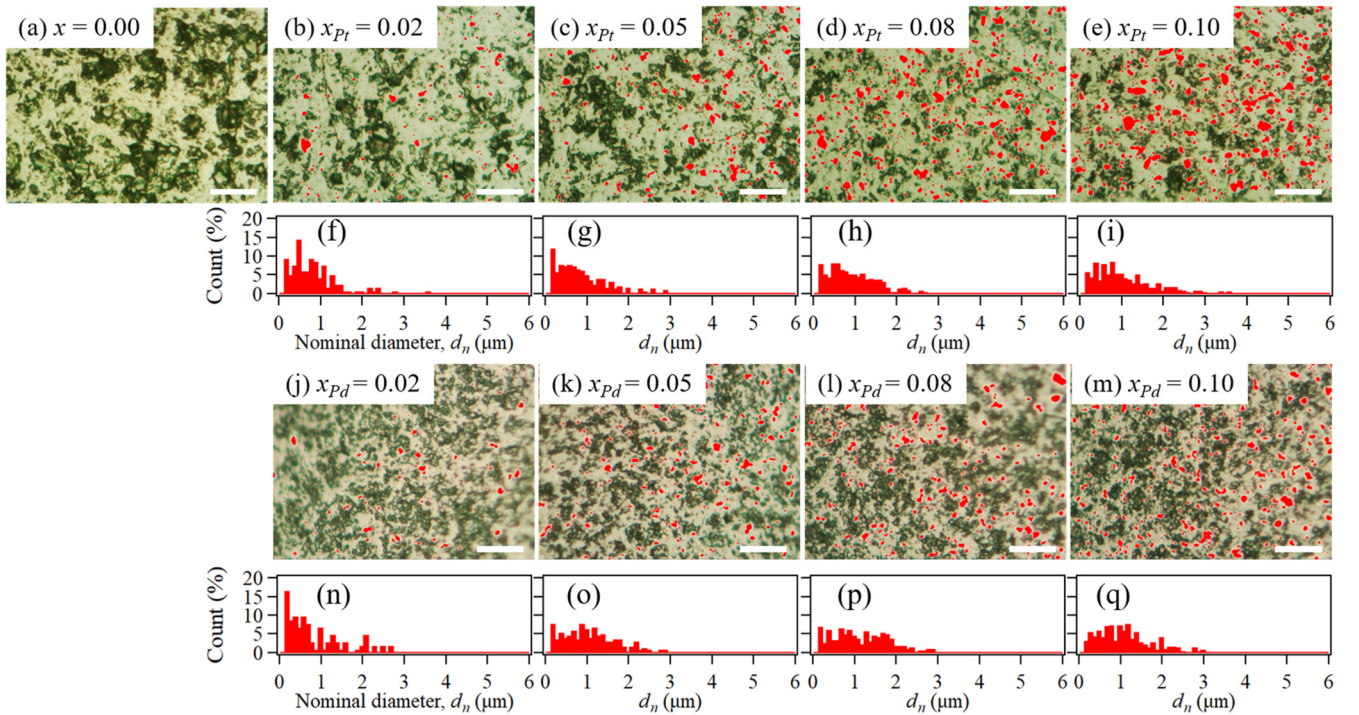| x_{Pt}	0.00	0.02	0.05	0.08	0.10
Packing ratio	0.96 ± 0.01	0.97 ± 0.01	0.95 ± 0.01	0.95 ± 0.01	0.98 ± 0.01
D_{ave} (μm)	0	0.65	0.75	0.97	1.12
x_{Pd}		0.02	0.05	0.08	0.10
Packing ratio		0.95 ± 0.01	0.95 ± 0.01	0.94 ± 0.01	0.95 ± 0.01
d_{ave} (μm)		0.90	1.15	1.21	1.32

FIG. 2. Optical microscope images of the surface of the $(NiO)_{1-x}HM_x$ samples. The polished surfaces of the $(NiO)_{1-x}Pt_x$ and $(NiO)_{1-x}Pd_x$ samples are shown in (a)–(e) and (j)–(m), respectively. The size of the scale bars is 25 μm. The HM granular areas are spotted by red by the image analysis described in the SM. The corresponding histograms of the nominal granular diameter d_n are shown in (f)–(i) and (n)–(q).

between 300 and 440 K. We apply no magnetic field in the measurements.

Figure 2 shows the optical microscope images of the polished surface of the NiO-HM granular pellets. Randomly dispersed HM granules are seen in the brightest color in the NiO matrix (the second brightest regions). The darkest regions are due to the surface roughness developed by surface abrasions during the polishing process (the raw images are found in the SM [29]). The HM granule regions are filled with red in Figs. 2(b)–2(e) and 2(j)–2(m) to make them more visible. Figures 2(f)–2(i) and 2(n)–2(q) show the corresponding histograms of the nominal diameter d_n of the granule (see the SM for the analysis of d_n). The average diameter of the HM granules d_{ave} were estimated and are summarized in Table I.

Figure 3 shows the x-ray diffraction (XRD) of the NiO-Pt and the NiO-Pd granular pellets with different compositions. We find two separate phases of pure NiO and pure Pt or pure Pd without any other impurity phases (see the SM for more extensive investigations on the intermixing [29]). The diffraction linewidths for the NiO, the Pt, and the Pd are too narrow to be analyzed by the Scherrer equation, giving only a rough estimation for the crystal grain size being >100 nm with which the finite-size effect is negligible [32]. There are no appreciable differences in the peak position (see the insets of Fig. 3) as well as the linewidths in all the samples, suggesting the inclusion of the HM granules does not influence the crystalline structures of the NiO.

The antiferromagnetic resonant mode at ∼1 THz, corresponding to the out-of-the-easy-plane mode [27], was seen in the transmission spectra for all the samples at room temperature and no other modes are apparent in the range of 0.1–2 THz. The temperature dependence of the resonant

frequency shown in Fig. 4 is nearly the same for all the samples, indicating that the HM granules in the NiO matrix do not influence the magnetic susceptibility, or the exchange constant [33], and the out-of-the-easy-plane anisotropy, both of which are relevant to the resonant frequency [31]. The Néel temperature and the resonant frequency at 0 K are estimated to be $T_N = 521 \pm 2$ K and $\omega_0/(2\pi) = 1.095 \pm 0.002$ THz, respectively, by the equation $\omega = \omega_0[M_0'(T)]^n$ where $(M_0'T)$ is the normalized sublattice magnetization computed

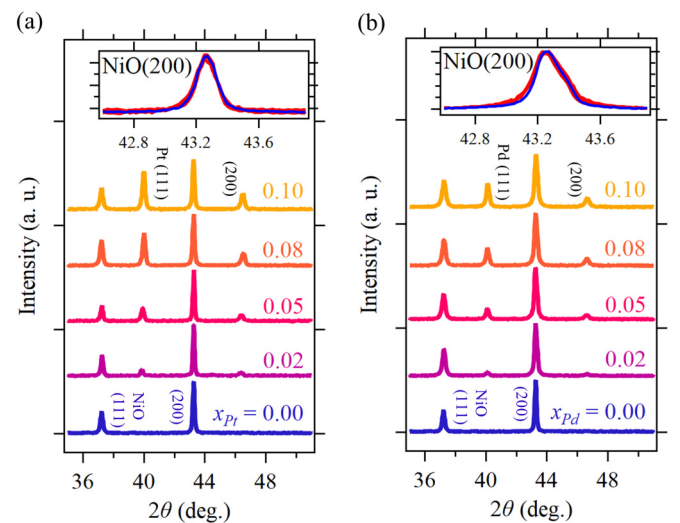FIG. 3. X-ray diffraction (XRD) and antiferromagnetic resonance. (a) XRD of the $(NiO)_{1-x}Pt_x$ samples. (b) XRD of the $(NiO)_{1-x}Pd_x$ samples. The insets magnify and superpose the NiO(200) peaks of all the compositions.

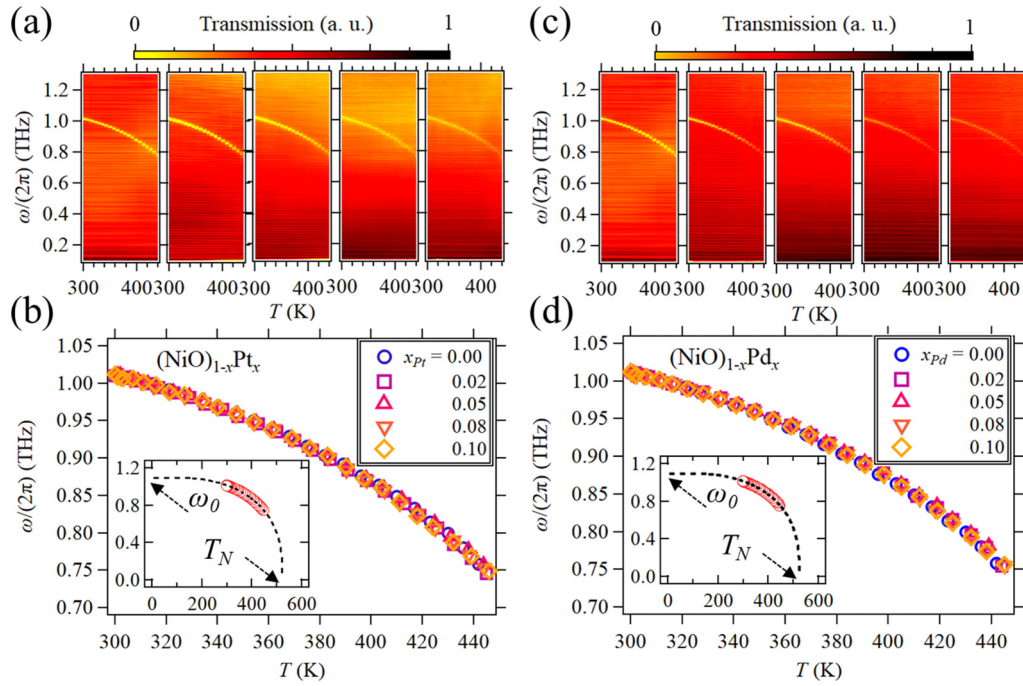FIG. 4. Transmission spectra of the (a) $(NiO)_{1-x}Pt_x$ and (c) $(NiO)_{1-x}Pd_x$ samples as functions of frequency and temperature. The resonant frequency as a function of temperature for the (b) $(NiO)_{1-x}Pt_x$ and (d) $(NiO)_{1-x}Pd_x$ samples. The insets in (b) and (d) superpose the resonant frequency of all the $(NiO)_{1-x}HM_x$ samples and the fitting curve to obtain T_N and ω_0.

by the Brillouin function $B_{S=1}(T)$ and $n = 0.72$ is the exponent for NiO [30,33]. These results prove that the quality of the NiO matrix is the same regardless of the HM granule inclusions. The resonant linewidth $\Delta\omega$ is obtained by fitting the absorption peak at 300 K with the Lorentzian function as shown in Fig. 5. By using the measured susceptibility $\chi = (1.49 \pm 0.01)\hbar \times 10^{-13}$ s/nm³ which translates into $\chi_\perp = (3/2)\chi = (2.24 \pm 0.01)\hbar \times 10^{-13}$ s/nm³ [29] and $s = 27\hbar$ nm⁻³ [25] for the NiO, the damping constant α is estimated by Eq. (6) and is shown in Fig. 6(a). It is evident that $\Delta\omega$ and α increase with increasing both x_{Pt} and x_{Pd}. α

increases much more rapidly with the Pt granular than the Pd granular.

We now address some caveats concerning the antiferromagnetic spin pumping model. We first need to ensure that the increase of $\Delta\omega$ and α is solely due to the effect of the HM granules. The major concern is extrinsic contributions to the damping, such as the inhomogeneous broadening [31], due to the inclusion of the HM granules. It is known that this extrinsic contribution can vary depending on the quality of the sample, such as defects, inhomogeneities, and crystallinity. The effect of crystallinity can be insignificant since the XRD indicates that the NiO maintains its inherent crystal structure regardless of the HM granular inclusions (see Fig. 3). On the other hand, a control experiment is necessary to address the effect of the HM granules viewed as defects and inhomogeneities in the NiO pellet. In order to create control samples with the same defects and inhomogeneities but without the HM granules, we prepared the NiO pellets with air pores, or *air granules*, the density x_p of which is in the same range as the
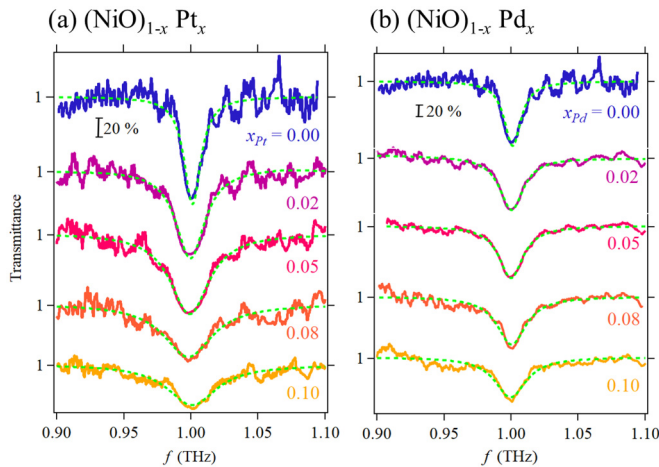

FIG. 5. x dependence of the transmittance spectra for (a) $(NiO)_{1-x}Pt_x$ and (b) $(NiO)_{1-x}Pd_x$. The dotted curve is the Lorentzian fitting from which the linewidth $\Delta\omega$ is obtained.
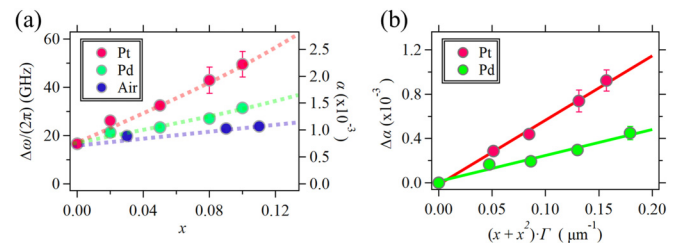

FIG. 6. (a) Linewidth $\Delta\omega$ and damping α as a function of x with the Pt, Pd, and air granules. The dotted curve is a guide to the eyes. (b) $\Delta\alpha$ as a function of $(x + x^2)\Gamma$ fitted with Eq. (7) to obtain g_{eff}.

HM granules (see the SM for the exact definition of x_p [29]). As the obtained $\Delta\omega$ and α almost stay constant with respect to x_p [see Fig. 6(a)], the defects and inhomogeneities by the air granules do not significantly contribute to the damping, which therefore ensures that the damping enhancement is predominantly due to the HM. We should note that our experimental setup does not have a mechanism to clearly distinguish the nonlocal effect, i.e., the spin pumping effect, from other "local" effects, such as the magnetic proximity effect, the spin memory loss [23,24], and the interfacial incoherent magnons [34,35], which could contribute to the damping enhancement. All these parasitic effects are inherently absorbed into the enhancement of our effective interfacial damping conductance g_{eff} ($\geqslant g_{\text{eff}}^{\uparrow\downarrow}$).

For convenience in analyzing the experimental data, we can rewrite Eq. (3) by taking into account the distribution of the nominal granular diameter d_n and the enhanced damping $\Delta\alpha = \alpha - \alpha_0 - \alpha_p(x)$ with $\alpha_0 = 7.4 \times 10^{-4}$ of $x = 0$ and the damping increase in air granular sample $\alpha_p(x)$ as

$$\Delta\alpha = \frac{3\hbar g_{\text{eff}}}{2\pi s}(x + x^2)\frac{\sum_n d_n^2 f_n}{\sum_n d_n^3}, \qquad (7)$$

where f_n is a factor relating the surface area of the ideal spherical granule with the diameter d to that of the actual irregular granule, which can be experimentally obtained from the image analysis of Fig. 2 (see the SM for a more detailed derivation of Eq. (7) [29]). Note that, from now on, we use $g_{\text{eff}}^{\uparrow\downarrow}$ to absorb the parasitic effects.

Figure 6(b) shows $\Delta\alpha$ as a function of $(x + x^2)\Gamma$, where $\Gamma = \sum_n d_n^2 f_n / \sum_n d_n^3$. The fitting with Eq. (7) yields the effective interfacial damping conductance to be $g_{\text{eff}} = 12 \pm 1 \, \text{nm}^{-2}$ and $5 \pm 1 \, \text{nm}^{-2}$ for the NiO/Pt and the NiO/Pd interfaces, respectively. The effective spin mixing conductance $g_{\text{eff}}^{\uparrow\downarrow}$ for antiferromagnets is generally expected to be of the same order of magnitude as the ferromagnetic counterpart [17], i.e., $\sim 10 \, \text{nm}^{-2}$, and similarly to the ferromagnetic case it is sensitive to interface quality. Most importantly, the Pd interface exhibits smaller g_{eff} than the Pt interface, which is in line with the $g_{\text{eff}}^{\uparrow\downarrow}$ behavior in the ferromagnetic/HM case. The latter is conventionally related to the spin-sink properties of the normal metal, as well as the magnetic proximity effect and spin relaxation at the interface [9,23,24]. Therefore, the trend of g_{eff} in the NiO/Pt and the NiO/Pd cases suggests that the spin pumping effect is present at the NiO/HM interface.

The g_{eff} found in this study, in good agreement with a general rough theoretical estimate of the effective spin mixing conductance $g_{\text{eff}}^{\uparrow\downarrow} \sim 10 \, \text{nm}^{-2}$ for antiferromagnets [5,17–19,36], is an important milestone in antiferromagnetic spintronics and particularly gives guidelines for various spin current transfer and spin interaction phenomena with antiferromagnets, which has recently been studied vigorously [4,5,36–38]. The most fascinating aspect of the antiferromagnetic spin pumping effect is the electrical detection of the antiferromagnetic spin dynamics in combination with ISHE, which leads to antiferromagnetic THz spin devices [17–20]. It, however, remains more challenging to realize an appreciable spin pumping voltage signal than to detect the damping enhancement in the present work since the former is proportional to θ^2, where θ is the cone angle of the precessing Néel order, which is generally expected to be much smaller than the ferromagnetic case [18]. We also note that, while the present experiments rely on the bulk THz absorption, it should be important in the interest of THz spintronics to develop those mechanisms suitable for thin film antiferromagnet systems.

In summary, we investigated the enhancement of antiferromagnetic damping in the NiO/HM system. Under the assumption of the spin pumping model, we estimate the effective interfacial damping conductance of the NiO/Pt and NiO/Pd interface to be $g_{\text{eff}} = 12 \pm 1 \, \text{nm}^{-2}$ and $5 \pm 1 \, \text{nm}^{-2}$, respectively. Our experimental results suggest the missing part of the spin interaction physics in antiferromagnets at THz, i.e., the spin pumping effect, among other possible parasitic effects such as the proximity effect and the spin memory loss. Although more intensive development should be necessary to demonstrate the electrical detection of the spin pumping effect with ISHE, which is challenging yet the most fascinating aspect of the antiferromagnetic spin pumping effect leading to THz spin devices [17–20], the present work which experimentally estimates g_{eff} encourages such research direction. Furthermore, the experimental manifestation of the value of g_{eff} helps in understanding various spin current transfer and spin interaction phenomena with antiferromagnets, and would further motivate and promote the antiferromagnetic spintronics.

[1] D. C. Ralph and M. D. Stiles, J. Magn. Magn. Mater. **320**, 1190 (2008).

[2] E. B. Myers, D. C. Ralph, J. A. Katine, R. N. Louie, and R. A. Buhrman, Science **285**, 867 (1999).

[3] S. I. Klselev, J. C. Sankey, I. N. Krivorotov, N. C. Emley, R. J. Schoelkopf, R. A. Buhrman, and D. C. Ralph, Nature (London) **425**, 380 (2003).

[4] X. Z. Chen, R. Zarzuela, J. Zhang, C. Song, X. F. Zhou, G. Y. Shi, F. Li, H. A. Zhou, W. J. Jiang, F. Pan, and Y. Tserkovnyak, Phys. Rev. Lett. **120**, 207204 (2018).

[5] T. Moriyama, K. Oda, T. Ohkochi, M. Kimata, and T. Ono, Sci. Rep. **8**, 14167 (2018).

[6] P. Wadley, B. Howells, J. Elezny, C. Andrews, V. Hills, R. P. Campion, V. Novak, K. Olejnik, F. Maccherozzi, S. S.

Dhesi, S. Y. Martin, T. Wagner, J. Wunderlich, F. Freimuth, Y. Mokrousov, J. Kune, J. S. Chauhan, M. J. Grzybowski, A. W. Rushforth, K. W. Edmonds, B. L. Gallagher, and T. Jungwirth, Science **351**, 587 (2016).

[7] T. Moriyama, W. Zhou, T. Seki, K. Takanashi, and T. Ono, Phys. Rev. Lett. **121**, 167202 (2018).

[8] N. Locatelli, V. Cros, and J. Grollier, Nat. Mater. **13**, 11 (2013).

[9] Y. Tserkovnyak, A. Brataas, G. E. W. Bauer, and B. I. Halperin, Rev. Mod. Phys. **77**, 1375 (2005).

[10] S. Mizukami, Y. Ando, and T. Miyazaki, Jpn. J. Appl. Phys. **40**, 580 (2001).

[11] E. Saitoh, M. Ueda, H. Miyajima, and G. Tatara, Appl. Phys. Lett. **88**, 182509 (2006).

[12] A. Brataas, Y. Tserkovnyak, G. E. W. Bauer, and B. I. Halperin, Phys. Rev. B **66**, 060404(R) (2002).

[13] K. Ando, S. Takahashi, J. Ieda, Y. Kajiwara, H. Nakayama, T. Yoshino, K. Harii, Y. Fujikawa, M. Matsuo, S. Maekawa, and E. Saitoh, J. Appl. Phys. **109**, 103913 (2011).

[14] J. C. Rojas Sánchez, L. Vila, G. Desfonds, S. Gambarelli, J. P. Attané, J. M. De Teresa, C. Magén, and A. Fert, Nat. Commun. **4**, 2944 (2013).

[15] T. Jungwirth, X. Marti, P. Wadley, and J. Wunderlich, Nat. Nanotechnol. **11**, 231 (2016).

[16] V. Baltz, A. Manchon, M. Tsoi, T. Moriyama, T. Ono, and Y. Tserkovnyak, Rev. Mod. Phys. **90**, 015005 (2018).

[17] S. Takei, B. I. Halperin, A. Yacoby, and Y. Tserkovnyak, Phys. Rev. B **90**, 094408 (2014).

[18] R. Cheng, J. Xiao, Q. Niu, and A. Brataas, Phys. Rev. Lett. **113**, 057601 (2014).

[19] Ø. Johansen and A. Brataas, Phys. Rev. B **95**, 220408(R) (2017).

[20] S. A. Gulbrandsen and A. Brataas, Phys. Rev. B **97**, 054409 (2018).

[21] J. Walowski and M. Münzenberg, J. Appl. Phys. **120**, 140901 (2016).

[22] D. M. Mittleman, J. Appl. Phys. **122**, 230901 (2017).

[23] Y. Liu, Z. Yuan, R. J. H. Wesselink, A. A. Starikov, and P. J. Kelly, Phys. Rev. Lett. **113**, 207202 (2014).

[24] M. Caminale, A. Ghosh, S. Auffret, U. Ebels, K. Ollefs, F. Wilhelm, A. Rogalev, and W. E. Bailey, Phys. Rev. B **94**, 014414 (2016).

[25] M. T. Hutchings and E. J. Samuelsen, Phys. Rev. B **6**, 3447 (1972).

[26] A. F. Andreev and V. I. Marchenko, Sov. Phys. Usp. **23**, 21 (1980).

[27] T. Satoh, S.-J. Cho, R. Iida, T. Shimura, K. Kuroda, H. Ueda, Y. Ueda, B. A. Ivanov, F. Nori, and M. Fiebig, Phys. Rev. Lett. **105**, 077402 (2010).

[28] Y. Tserkovnyak and H. Ochoa, Phys. Rev. B **96**, 100402(R) (2017).

[29] See Supplemental Material at http://link.aps.org/supplemental/10.1103/PhysRevB.101.060402 for extended description and data.

[30] A. Roggenbuck, H. Schmitz, A. Deninger, I. C. Cámara Mayorga, J. Hemberger, R. Güsten, and M. Grüninger, New J. Phys. **12**, 043017 (2010).

[31] T. Moriyama, K. Hayashi, K. Yamada, M. Shima, Y. Ohya, and T. Ono, Phys. Rev. Mater. **3**, 051402 (2019).

[32] R. H. Kodama, S. A. Makhlouf, and A. E. Berkowitz, Phys. Rev. Lett. **79**, 1393 (1997).

[33] A. Sievers and M. Tinkham, Phys. Rev. **129**, 1566 (1963).

[34] B. Flebus, P. Upadhyaya, R. A. Duine, and Y. Tserkovnyak, Phys. Rev. B **94**, 214428 (2016).

[35] C. Du, T. van der Sar, T. X. Zhou, P. Upadhyaya, F. Casola, H. Zhang, M. C. Onbasli, C. A. Ross, R. L. Walsworth, Y. Tserkovnyak, and A. Yacoby, Science **357**, 195 (2017).

[36] H. Wang, C. Du, P. C. Hammel, and F. Yang, Phys. Rev. Lett. **113**, 097202 (2014).

[37] C. Hahn, G. Loubens, V. V. Naletov, J. B. Youssef, O. Klein, and M. Viret, Europhys. Lett. **108**, 57005 (2014).

[38] T. Moriyama, S. Takei, M. Nagata, Y. Yoshimura, N. Matsuzaki, T. Terashima, Y. Tserkovnyak, and T. Ono, Appl. Phys. Lett. **106**, 162406 (2015).